REVIEW OF SCIENTIFIC INSTRUMENTS VOLUME 74, NUMBER 11 NOVEMBER 2003

Imaging the high-speed impact of microdrop on solid surface

Ho-Young Kim
Thermal/Flow Control Research Center, Korea Institute of Science and Technology, Seoul 136-791, Korea
Soon-Young Park
Space Propulsion Division, Korea Aerospace Research Institute, Daejun 305-333, Korea
Kyoungdoug Min[a]
School of Mechanical and Aerospace Engineering, Seoul National University, Seoul 151-742, Korea

(Received 8 April 2003; accepted 11 August 2003)

An experimental setup that images the high-speed impact of a microdrop onto solid surfaces is described. The drop generation system provides a stream of monosized microdrops having diameter near 100 μm and the velocity around 10 m/s. The drop train is manipulated to deliver a single drop onto a solid target by selective charging and deflection. The images of drop spreading at different times are obtained by the double-flash photography technique. Representative experimental results are given with the estimation error of time elapsed after impact below 5 μs. In addition, it is shown that drop impact kinematics can be adopted to estimate the time in the very early stages of drop spreading. Such drop delivery and optical imaging system can be used to study the fuel spray behavior in internal combustion engines and molten microdrop deposition process in droplet-based manufacturing. © *2003 American Institute of Physics.* [DOI: 10.1063/1.1614860]

I. INTRODUCTION

Impact of a liquid drop on a solid surface has been the subject of intensive study for more than a century.[1] The fluid dynamic behavior associated with drop impact, e.g., drop base diameter evolution, is determined by the impact velocity, the original drop diameter, the surface tension, the viscosity, and interfacial parameters such as contact angle and slip length.[2] When the effects of the interfacial parameters are neglected in the inertia-dominating spreading stage, the fluid dynamic behavior is determined by the Weber number and the Reynolds number, defined, respectively, as $\mathrm{We}=\rho U^2 D/\sigma$ and $\mathrm{Re}=\rho UD/\mu$. Here ρ, σ, and μ denote the drop density, the surface tension, and the viscosity, respectively, D is the drop diameter and U is the impact velocity. If heat transfer is involved in addition to fluid dynamics, relevant nondimensional parameters such as the Prandtl number and solid–liquid property ratios are added. Furthermore, when the phase change of a drop accompanies, one should include the Stefan number and drop superheat parameter in the group of relevant parameters. When multiple dimensionless parameters affect the drop impact behavior, a specific experimental condition can hardly be generalized by virtue of the similarity argument. Therefore, in order to understand the thermal or fluid-dynamic impact behavior of a certain condition, it is inevitable to perform experiments corresponding to the specific impact conditions.

The understanding of liquid drop impact comes mainly from observing drop morphology evolution during its interaction with a solid target. Unless a highly viscous drop is gently placed on a solid, drop impact phenomena are usually too rapid to be seen by either naked eyes or ordinary CCD cameras operated at the speed of 30 frames per second. The time scale of inertia-controlled drop spreading, τ, can be estimated by $\tau = D/U$. Supposing that a syringe generates a drop of 2 mm diameter, 30 cm above a solid target, the impact velocity is approximately 2.4 m/s neglecting air resistance. Then the impact process takes place within about 1 ms. To obtain the temporal evolution of physical parameters, such as the base diameter or height, during spreading, the temporal resolution of the imaging technique should be much less than τ. In the aforementioned case, the imaging system should be able to capture the process with the resolution of 100 μs or so. Such a high temporal resolution can be achieved by commercial high speed cameras which can be operated as fast as over 40 000 frames per second,[3] but they usually suffer from poor image quality as well as short recording period.

The difficulty can be circumvented in two ways. One can investigate the impact process with a greater τ by using a larger drop or reducing the drop velocity. Then the drop impact process can be imaged with a high speed video camera running at the speed of the order of 1000 frames per second.[4] In addition to high speed video system, the stroboscope or an arc lamp with an ultrashort flash duration enables one to capture sharp images of rapidly moving objects at prespecified instances. In drop impact studies using this technique, usually an optical sensor, situated between a drop generator and a target, detects a traveling drop and provides electrical signal to trigger the flash[5,6] or camera shutter[7] after a given delay time. One can reconstruct the drop impact process by taking multiple pictures of different drops while varying the time delay based on the assumption that the drop impact conditions are reproduced exactly. When using a large drop in experiments, however, the reproducibility of experimental

---

[a] Author to whom correspondence should be addressed; electronic mail: kdmin@snu.ac.kr

TABLE I. Typical impact conditions experimentally investigated to date.

Reference	Liquid	D (mm)	U (m/s)
4	water, ink, silicone oil	2.8–3.5	0.77–3.47
5	*n*-heptane	1.5	0.93
6	water	5.5	2.4–4.0
7	water	2.7	1.58–4.53
8	water, glycerin, silicone oil	1.2–4.9	0.78–4.1
12	molten solder	0.08	1.5
24	water	0.45	2.7
26	water	23	0.63–2.20

conditions is in serious doubt especially because the drop is not spherical at impact due to its oscillation.[6] On the other hand, when the drop size is in submillimeter scales, the drop rapidly recovers the spherical shape after a few oscillation periods upon exiting the drop generator nozzle. The refinement to the flash photography can be devised by executing multiple exposure for a CCD camera[8] although the images of the spreading drop are overlapped in one image. Using the imaging techniques surveyed above, the impact dynamics of drops having diameters from approximately 100 μm to 4 mm and velocities on the order of 1 m/s have been imaged so far. This experimental range covers natural processes such as raindrops hitting a windowpane and industrial processes such as solder jet bumping.[9] Some typical experimental conditions employed so far are listed in Table I.

In this work, we aim to provide an experimental apparatus and technique for a microdrop $[O(D)=10-100\ \mu\text{m}]$ impacting on a solid surface with a high velocity $[O(U)=10\ \text{m/s}]$. This experimental condition is of great practical importance since it can simulate a fuel spray impacting on diesel or spark-ignited engine walls[10] or a rapid prototyping process using molten metal microdrops.[11] As mentioned above, the rigorous experimental understanding of such a process involving both fluid dynamics and heat transfer can only be obtained by realizing the exact impact conditions. However, no experimental studies have been reported of the high-speed impact of microdrops thus far, and here we present the imaging results of such impact conditions. The experimental setup constructed in this work consists of a device to provide a single microdrop having a high impact speed and an imaging system with the temporal resolution of less than 10 μs. In the following we describe the development of those experimental systems consisting of microdrop generator/manipulator and high-speed photography setup. Then we present representative experimental results obtained by using the described system.

II. GENERATION AND MANIPULATION OF MICRODROPS

A. Apparatus

We develop a microdrop-generation system which delivers a single microdrop with a high velocity onto a solid target. A single drop with a diameter of approximately 100 μm can be produced by ejecting a small liquid mass through a micronozzle. The ejection can be realized by pressurizing a liquid chamber instantaneously with a thermal bubble or piezoelectric membrane, and this mode of drop generation is referred to as drop-on-demand. However, the drop-on-demand method typically produces a drop having a low velocity (around 1 m/s).[12] To produce a microdrop with a large traveling speed, a continuous liquid jet should be ejected from a nozzle. A liquid jet is inherently unstable under capillary action and this phenomenon is commonly called the Rayleigh instability.[13] If a periodic disturbance is given to the jet, it is broken up into a train of drops of identical size and velocity. This method of drop generation is referred to as the continuous-jet mode and has been exploited for various applications such as inkjet printing,[14] solder ball production,[15] and free-form fabrication.[11]

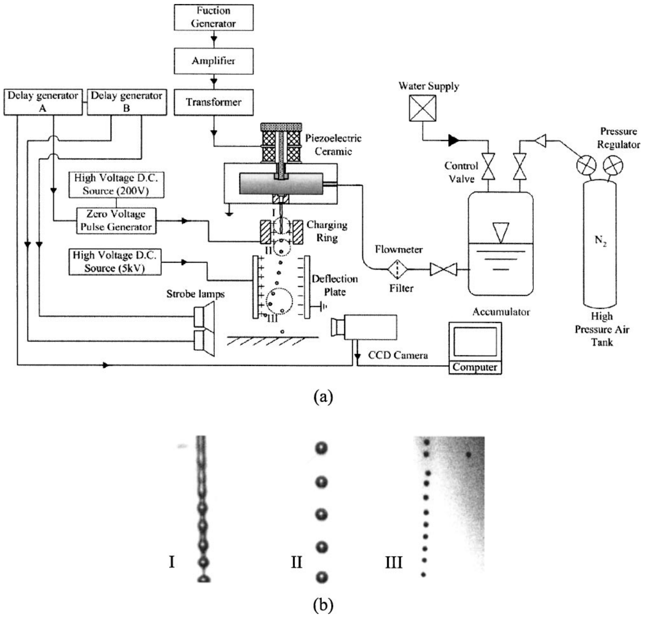

FIG. 1. (a) Schematic of experimental apparatus; (b) drop images at regions I, II, and III as designated in (a).

We fabricate a microdrop generator consisting of a liquid chamber, piezoelectric vibration unit, and an orifice. A schematic of the setup is shown in Fig. 1. The liquid chamber is supplied with distilled water pressurized by air. The liquid is ejected through a ruby orifice whose diameter can vary between about 10 μm and 2 mm (Bird Precision), and is given a periodic forcing by the piezoelectric vibrator. The vibrator is driven by an alternate current amplifier connected to a function generator (Stanford Research Systems DS-345). When the jet radius is a and the undulation on the liquid jet has the wavelength λ, the diameter of the resulting drop D becomes $D=(6a^2\lambda)^{1/3}$ by volume conservation. λ is related to the jet velocity, v_j, and vibration frequency, f, as $\lambda=v_j/f$. Figure 1 includes the image of microdrops emerging from a continuous water jet.

For the microdrop generator to serve the purpose of the single drop impact study, the drop stream should be manipulated to deliver only a single drop onto a target. We isolate a single drop by electrically deflecting the drop stream except only one drop. This is similar to a scheme of flow cytometry in which an optical system detects a specific biological substance contained in drops generated by continuous-jet mode and those drops are selectively deflected to be separated from the other drops.[16] In our experiments, we deflect all the drops into a gutter except a single drop which is allowed to fall straight onto a target. To this end, the charging and deflecting apparatus are situated beneath the orifice as shown in Fig. 1. The charging ring connected to the high-voltage power supply induces electrical charge on drops and those drops are veered off the straight path by the deflection plates. Unlike the deflection plates where the constant electric field is maintained throughout the experiment, the charging ring is connected to a circuit that grounds the ring for a short time on demand. A microdrop which forms from the liquid jet during the shutoff period is not charged and thus travels straight unaffected by the deflecting field downstream. This microdrop collides with the target and we image its collision behavior.

B. Analysis

To effectively induce electrical charge on drops, it is important to place the charging ring at the jet breakup location. The jet breakup length, l_j, is the distance from the orifice where the initial disturbance sets in, to the breakup location. It corresponds to the traveling distance of the liquid jet for the time t^* until the magnitude of the disturbance grows to equal the jet radius a. Therefore, a and t^* are related as, under the linear stability assumption:[17]

$$a = \eta_0 \exp(qt^*), \tag{1}$$

where η_0 is the magnitude of the initial disturbance and q the growth rate of the disturbance of the wavelength $\lambda_{\max}$. Using $l_j = v_j t^*$, we get

$$l_j = \frac{v_j}{q} \ln(a/\eta_0). \tag{2}$$

It is practically impossible to know the value of η_0 *a priori*, which is supposed to be infinitesimal. Hence, we experimentally determine its value, or $\ln(a/\eta_0)$ for $v_j = 5.35$ m/s and $a = 50\,\mu$m. The growth rate q is predicted from the linear stability theory. Weber's theory[18] gives q as:

$$q^2 + \frac{3\mu\xi^2}{\rho a^2} q = \frac{\sigma}{2\rho a^3}(1-\xi^2)\xi^2 + \frac{U\rho_a \xi^3 K_0(\xi)}{2a^2\rho K_1(\xi)}, \tag{3}$$

where μ is the drop viscosity, $\xi = 2\pi a/\lambda$, ρ_a the air density, and K_n the modified Bessel function of the second kind, of order n. The value of λ is given by v_j and f, thus ξ and q are determined in sequence. Then measuring l_j yields the value of $\ln(a/\eta_0) = 8300$ for the condition tested. To test the generality of this value, we measure l_j for different experimental conditions and compare them with theoretical predictions in Fig. 2. We find that regardless of the jet velocity variation, the constant value of $\ln(a/\eta_0)$ can be employed to estimate l_j.

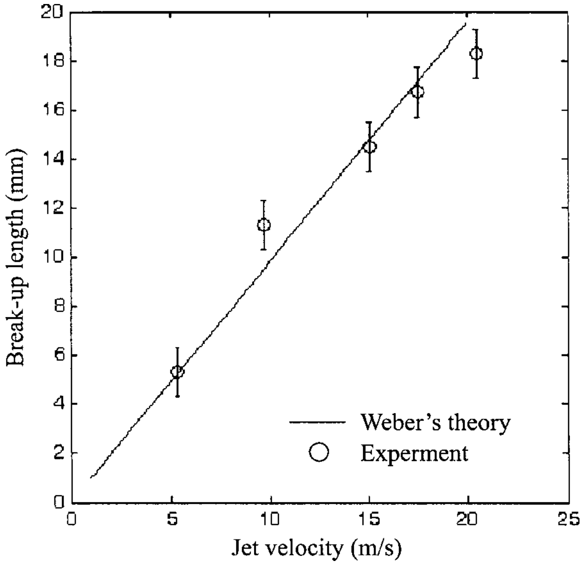

FIG. 2. Variation of jet breakup length with jet velocity.

The degree of drop stream deflection determines the location of the gutter. It is dependent on the electrical charge induced on each drop and the strength of electrical field in the deflection region. The net electrical charge on a drop is assumed to be identical to the electrical charge induced on the surface of a liquid column of length λ. Schneider *et al.*[19] modeled the liquid column and the surrounding charging ring as concentric cylindrical capacitors, and obtained the electrical charge Q per unit mass:

$$\frac{Q}{m} = \frac{2\pi\epsilon_0 V_c}{\rho a^2 \ln(r_c/a)}, \tag{4}$$

where m denotes the drop mass, ϵ_0 the permittivity of free space, V_c the charging voltage, and r_c the inner radius of the charging ring. Charged drops are veered off the original straight path due to the electric field in the deflection region. The drop trajectory is obtained by considering forces acting on the drop, i.e., gravity, air drag, and the electrostatic force. The equation of motion thus becomes

$$m\frac{d\overline{v}}{dt} = m\overline{g} + \overline{F_D} + Q\overline{E}, \tag{5}$$

where $\overline{v}$ is the drop velocity vector, t the time, $\overline{g}$ the gravitational acceleration, $\overline{F_D}$ the drag force, and E the electric field whose magnitude is given by $E = V_d/s$, V_d and s being the deflection voltage and the spacing between the deflection plates, respectively. The drag force F_D is written as $F_D = C_D \rho_a v^2 A/2$, where C_D is the drag coefficient and A the cross-sectional area of the drop. Orme *et al.*[20] used the drag coefficient for a single sphere to solve Eq. (5), but in reality, the drops move in an aligned train thus experience less drag than an isolated drop. Therefore, we use the drag coefficient given by Mulholland *et al.*[21] for the monodisperse droplet stream. Their model proposes the drag coefficient C_D for a drop traveling in a drop stream with the uniform spacing l_s as

$$\begin{aligned}[C_D(\mathrm{Re}_D, l_s/D)]^{-p} = {} & [C_D^0(\mathrm{Re}_D, l_s/D)]^{-p} \\ & + [C_D^\infty(\mathrm{Re}_D)]^{-p},\end{aligned} \tag{6}$$

where Re_D is defined as $\mathrm{Re}_D = UD/\nu_a$ with ν_a being the air's kinematic viscosity, the empirical constant $p = 0.678$, C_D^0 is the asymptotic value of C_D as $l_s/D \to 1$, and C_D^∞ is the drag coefficient for an isolated drop. C_D^0 is written as

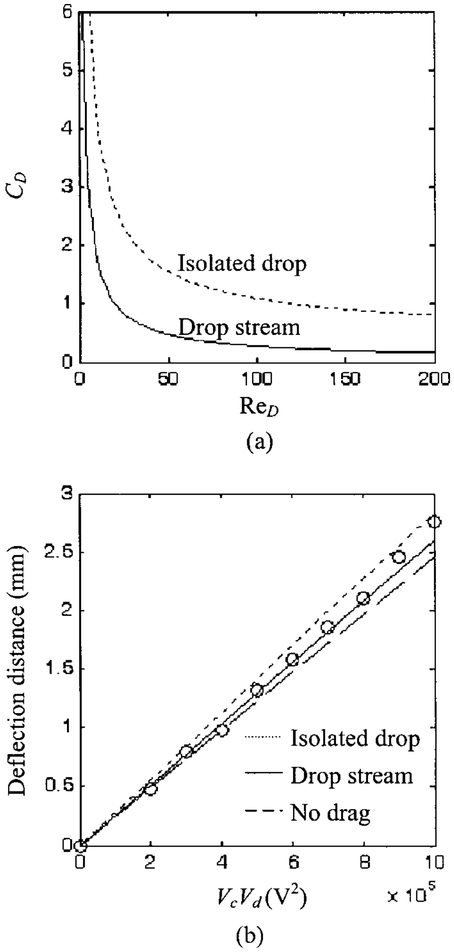

FIG. 3. Drag coefficient and deflection distance of traveling drop stream. In the experiments, $D = 300\ \mu\mathrm{m}$, $U = 5.35$ m/s, and $l_s/D = 2.3$. (a) Drag coefficient for isolated drop and drop stream. (b) Comparison of simulated and measured (circles) deflection distances. The drop stream simulation result lies between the predicted deflection distances for isolated drop and without air drag, and agrees well with the experimental results.

$$C_D^0(\mathrm{Re}_D, l_s/D) = C_D^{0'}(\mathrm{Re}_D) + e\,\mathrm{Re}_D^{-1}(l_s/D - 1), \tag{7}$$

where the empirical constant $e = 43.0$ and $C_D^{0'}$ is the drag coefficient when $l_s/D = 1$ expressed by $[C_D^{0'}(\mathrm{Re}_D)]^{-p} = [C_{\mathrm{rod}}(\mathrm{Re}_D)]^{-p} - [C_D^{\infty}(\mathrm{Re}_D)]^{-p}$. C_{rod} is the drag coefficient for an infinitely long cylinder and C_D^{∞} is given by[22]

$$C_D^{\infty} = 0.28 + \frac{6}{\mathrm{Re}_D^{1/2}} + \frac{21}{\mathrm{Re}_D}. \tag{8}$$

The location of the charged drop is obtained by numerically integrating Eq. (5) and the result is compared with the experimental measurements in Fig. 3. The figure also includes the results using the isolated drop model which overestimates the drag force.

III. DOUBLE-FLASH DIGITAL PHOTOGRAPHY

Since the microdrops delivered through the above scheme spreads very rapidly upon impacting on a solid surface with high speed, we reconstruct a sequence of drop spreading by taking photographs of drops having identical impact conditions at different times after impact. To obtain sharply frozen images of moving drops, a flash with a short duration should be triggered at a specified moment. As the drop size reduces to the order of 100 μm and the drop velocity reaches over 10 m/s, optical means to detect the drop for triggering often fails. Therefore, we synchronize the charging circuit with two stroboscopes, so that the strobes are triggered with a given delay by a signal grounding the charging ring for a short period. Two lamps are used to acquire the drop spreading image and also to measure the time elapsed after impact.

Hatta *et al.*[23] and Fujimoto *et al.*[24] used such double flashes to capture drop spreading images. Hatta *et al.* used a rotating disk with a slit to separate a drop from a stream of drops but no actual images are shown in their work.[23] Fujimoto *et al.* utilized essentially the same apparatus as Ref. 23 but they separated three successive drops from a drop stream to image the successive drop collision. Those studies suffered from the poor reproducibility of drop impact conditions due to air flow caused by the rotating disk. On the other hand, our drop delivery system exhibits an excellent reproducibility of impact conditions as discussed below.

A schematic of the imaging setup used in our study is included in Fig. 1. The imaging system consists of a CCD camera (PCO Pixelfly; 1280×1024 pixels), two delay generators (Stanford Research Systems DG-535), and two stroboscopes (Seolim DX-525). As shown in Fig. 1, delay generator A sends a signal to a power circuit upon manual command to shut off the charging for a short period. Delay generator A opens the shutter of the CCD camera after a delay time, τ_1, during which the drop approaches the target. While the camera shutter is kept open, delay generator B sparks the first strobe before the drop hits the target. After a delay time, τ_2, the second strobe is sparked by delay generator B. Then the camera shutter is closed by a software in which the CCD exposure duration is prescribed. By repeating the above procedure while changing τ_2, which is set to capture the drop image after impact, a sequence of drop images can be reconstructed. Each photograph of the CCD camera, digitally acquired by a personal computer equipped with a frame grabber, contains two images of the same drop at different moments, each corresponding to the moment before and after impact. With the drop velocity U known, the distance between the preimpact drop and the target surface, L, allows one to calculate the time taken for the drop to travel until impact, $\tau_3 = L/U$. Then $\tau_e = \tau_2 - \tau_3$ is the time elapsed after impact when the second drop image is taken. Here we emphasize that the elapsed time after impact is obtained only by using each image that contains two drop images before and after impact, without resorting to information of the drop delivery process.

Since the high-speed impact of small drops occurs within a very short time, a high degree of reproducibility is required to capture the images with sufficiently high temporal accuracy and resolution. Therefore, we measure the drop diameter and impact velocity to test the reproducibility of drop impact conditions provided by our drop generator. The impact velocity is measured by taking two images of the same drop both before impact in one frame as shown in Fig. 4. The impact velocity is calculated based on the prespecified

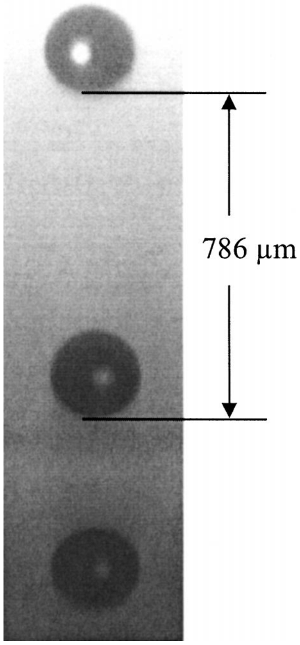

FIG. 4. Microdrop images used for measurement of impact velocity (case I). The images are of the same drop taken at different moments and the drop travels downward. The bottom-most drop image is the reflection from the solid surface.

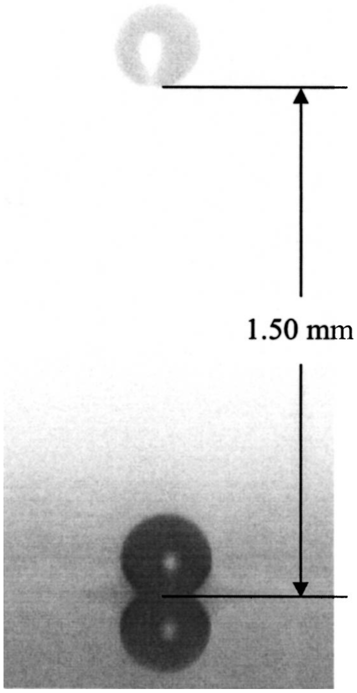

FIG. 5. Drop images to enable the estimation of drop impact moment. The drop impact conditions correspond to case II.

delay time and the measured distance between the drop images. Table II shows the measurement results in typical runs using the orifice of 100 μm diameter. Both the drop diameter and impact velocity are reproduced within a few per cents of standard deviation when at least 15 images are analyzed for each condition.

The temporal error of the current imaging system is determined by such factors as the precision of time delays generated by the delay generators, the strobe flash durations and the prediction accuracy of drop impact moment. The precision of delay is within 50 ps according to the manufacturer. We measure the strobe flash duration by sparking the flash and subsequently opening the camera shutter with a set interval using the delay generator. When the interval reaches 1.5 μs, the image taken by the camera is completely dark while the image is brightly saturated when the interval is 1 μs. Therefore, we find that the maximum flash duration of each strobe is less than 1.5 μs. The accuracy of the hitting moment estimation is dependent on the measurement errors of U and L, and the error associated with U is discussed above. The distance between the bottom of drop image before impact and the target surface is 480 pixels, or 1.50 mm, for the image shown in Fig. 5 and the measurement error is estimated to be ± 1 pixel ($\pm 0.21\%$). The distance a drop travels during a single strobe flash is less than 0.024 mm, thus its effect on the velocity measurement error is below 1.6%. Therefore, the error associated with estimating the moment of impact is evaluated to be less than 3.5 μs considering the error propagation (2 μs)[25] and flash duration (below 1.5 μs). Therefore, the maximum error associated with determining the time at which the second drop image is taken is below 5 μs. The magnitude of error is not negligible for the impact condition considered especially in the initial spreading stages. The error can be significantly reduced by using lamps with shorter flash duration and by increasing number of pixels corresponding to the drop travel distance. The current state-of-the-art of xenon flash lamp achieved the flash duration of 0.15 μs,[12] and its use can reduce the error to less than 2.3 μs. In addition to the methods described so far, the time elapsed after impact can be estimated by resorting to the drop impact kinematics. A further discussion of this method is given below.

TABLE II. Drop impact conditions. Std. denotes the standard deviation.

Case	D (μm)	Std. of D in μm (%)	U (m/s)	Std. of U in m/s (%)	We	Re
I	213	3.7(1.7)	8.0	0.13(1.6)	190	1700
II	260	4.5(1.7)	15.0	0.31(2.1)	810	3900
III	234	8.3(3.5)	16.2	0.21(1.3)	860	3800

IV. EXPERIMENTAL RESULTS

In this section, we present the representative experimental results obtained by the microdrop generation and imaging system discussed above. Figure 6 shows the images of a water drop of 260 μm diameter impinging on a polycarbonate surface with the impact velocity of 15.0 m/s. The time scale of inertial spreading period, τ, is about 17 μs for the current impact condition. The drop is shown to rapidly collapse into a thin disk of approximately 40 μm thickness for about 30 μs after impact. Upon reaching the maximum spreading degree, the drop recoils due to capillarity while increasing the disk thickness. After about 400 μs, the center of the recoiling drop rises resembling a dome. The dome rises with the increase of its volume while the fringe layer is drawn inward. Beyond 600 μs, the contact area is kept con-

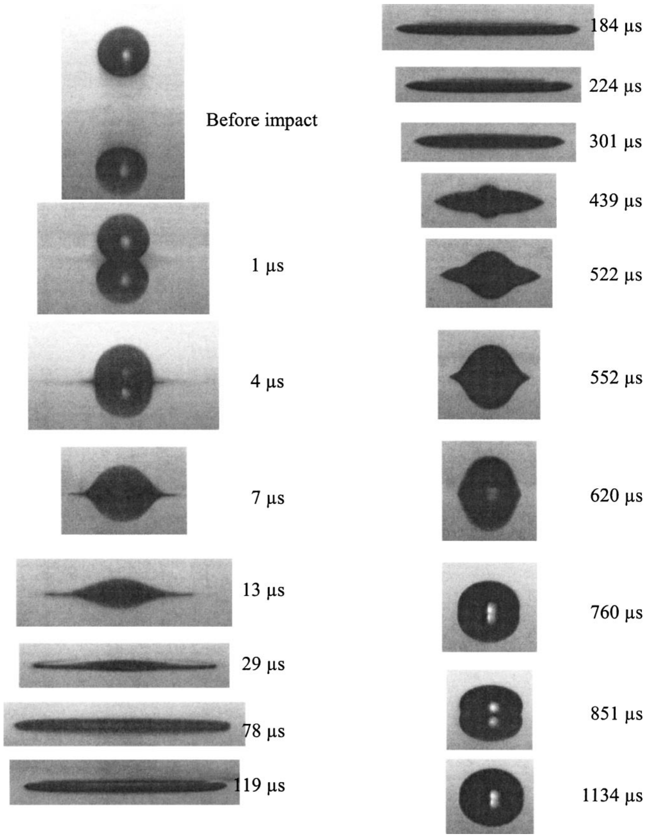

FIG. 6. Sequential images of microdrop impacting on polycarbonate surface with high speed. In the image before impact, the bottom drop image is the reflection of the upper. The drop impact conditions correspond to case II.

stant although the oscillation of the top surface continues even after 1 ms. The overall morphology evolution exhibits a similar trend to that of macrosized drops except that the current process takes place within a very short period of time. Figure 7 shows the spreading diameter evolution with time.

The relative accuracy of time estimation improves as the time increases since the magnitude of error is constant. However, in the very early stage of impingement, the error is not negligible compared with the estimated time. In this time range, another method based on the physics of drop impact can be resorted to for confirming the time estimation. According to Rioboo *et al.*,[8] the drop impact process consists of the kinematic phase and the subsequent spreading phase. The kinematic phase, corresponding to the very early stage of impact, is characterized by the absence of peripheral lamella. During this phase, the information of drop bottom contacting a solid surface yet propagates to the top and the liquid near the contact area is compressed. Hence the drop collapse speed is the same as the impact velocity. The second image in Fig. 6 shows such drop configuration in which the drop appears as a truncated sphere without lamella ejection. The measurement of the drop height reveals the time elapsed after impact to be 1.1 μs based on kinematics. A close look at the same image further shows that a vague image of lamella ejection is captured surrounding the drop bottom. This is supposed to be the event occurring while the lamp flashes for less than 1.5 μs. Combining these observations, we find that the kinematic phase lasts at least 1.1 μs upon impact and that the lamella starts to be ejected, i.e., the spreading phase ensues, in less than 2.6 μs upon impact.

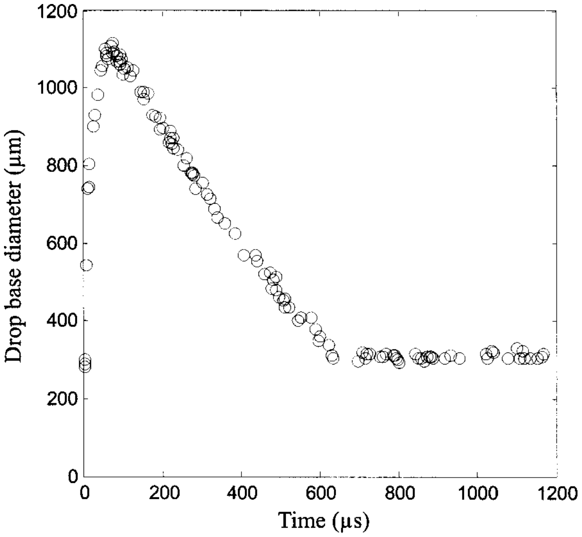

FIG. 7. Evolution of dimensional drop base diameter with time for case II.

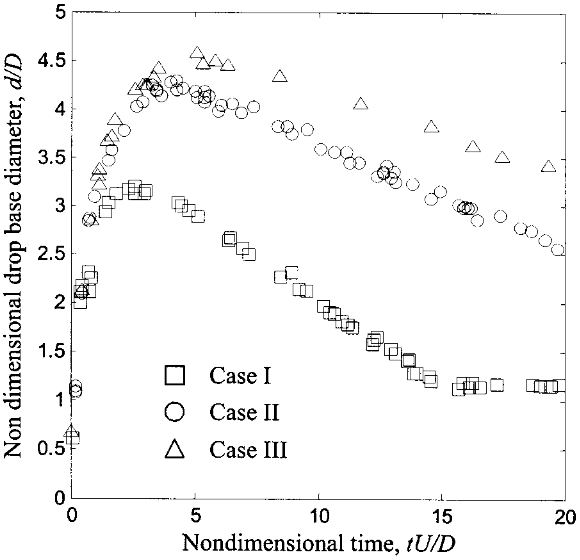

FIG. 8. Comparison of dimensionless drop base diameter evolutions for different impact conditions.

The third and fourth images exhibit the typical lamella ejection in the spreading phase. Reference 6 found that the drop collapse speed is almost the same as the original impact speed even after the kinematic phase until the time reaches $\tau/2$, and it corresponds to 8.5 μs in our case. Then measuring the drop height reduction again gives the time elapsed after impact. Thus obtained times for the third and the fourth images are 3.9 and 7.3 μs, respectively. We find these values are very close to the times inferred from measuring the drop location before impact imaged by dual flash.

The effects of impact conditions on the microdrop spreading behavior are investigated by measuring the images obtained using the conditions listed in Table II. The evolution of the spreading diameter $d(t)$ is plotted with the time t in dimensionless forms in Fig. 8. It is found that the drops with high impact speeds (cases II and III) spread more than one with low impact speeds (case I), which is consistent with

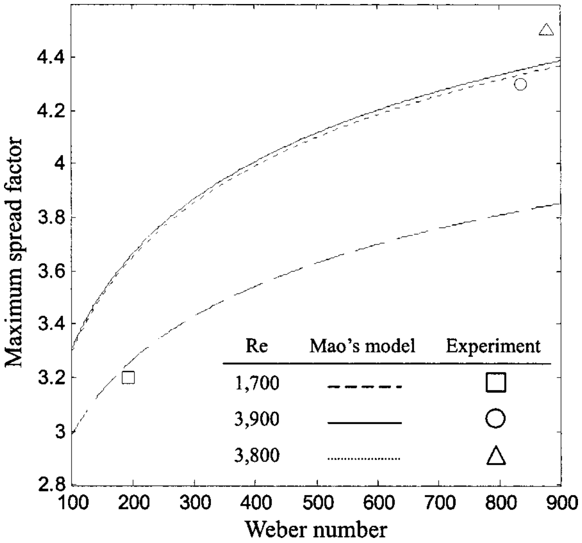

FIG. 9. Maximum spread factors predicted by Mao's model and measured by experiments.

the results of previous studies. In addition, the spreading phase is prolonged as the Weber number increases, thus the dimensionless time at which the maximum spreading degree is reached increases as the drop spreads more. We compare the maximum spreading degrees measured in the current experiments with the model of Ref. 7. The model is based on the assumption that the initial kinetic and surface energy of a drop is converted into viscous dissipation and the surface energy of the drop at the maximum spread state. The maximum spread factor, $\xi = D_m/D$, where D_m is the maximum diameter of the drop base, is the solution of the following equation:

$$\left[\frac{1}{4}(1-\cos\theta)+0.2\frac{\mathrm{We}^{0.83}}{\mathrm{Re}^{0.33}}\right]\xi^3-\left(\frac{\mathrm{We}}{12}+1\right)\xi+\frac{2}{3}=0. \quad (9)$$

Figure 9 compares the experimental results with the modeling. The predictions are in fairly good agreement with the measurements, which confirms that Eq. (9) provides adequate estimation of the maximum spread factor for high-speed impact of microdrops. However, it is noteworthy that our experimental results indicate that the maximum spread factor for case III having a higher Weber number is greater than that of case II although the modeling predicts almost identical values. It implies that the Weber number plays more important roles than the modeling assumes in this regime of drop impact. Further theoretical elaboration is called for to explain this observation.

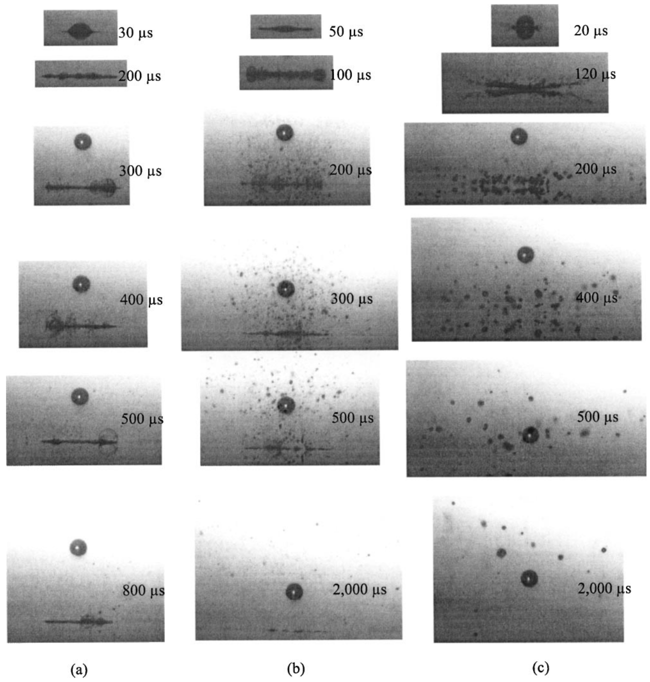

FIG. 10. Sequential images of microdrop hitting a hot aluminum surface. Original drop diameter is 235 μm and the impact velocity is 10 m/s. The spherical drop image above the surface and the spreading film are of the same drop. The solid surface temperature is (a) 150, (b) 200, and (c) 300 °C.

In addition to the experiments using a solid target at room temperature, we image the microdrop impact behavior onto a heated target. As discussed above, when heat transfer is involved in the impact process, the number of similarity variables increases thus extending the macroscale experimental results to microscale phenomena is impractical. In the experiments, a heated aluminum plate, whose root mean square (rms) surface roughness is below 0.1 μm, is used as a target. Images of water drops with the diameter of 235 μm and the impact velocity of 10.0 m/s are taken with the target surfaces maintained at constant temperature of 150, 200, and 300 °C. Figure 10 shows those images. It is noticed that the drop behavior is different for varying target temperature. When the target temperature is 150 °C, localized boiling occurs before 300 μs to form a growing thermal bubble out of the spread film. The formation and bursting of bubbles continue until the surface is completely dried out. Such formation of bubbles out of the liquid film has not been reported in millimeter-sized drops impacting on hot surfaces.[5,26–28] As the target temperature is raised to 200 °C, boiling gets so vigorous that the entire film is affected. Vigorous boiling results in the emission of tiny droplets vertically upward and the emitted droplets evaporate in the air without touching the hot surface. When the target temperature reaches 300 °C, which is above the Leidenfrost temperature (277 °C) of water, the spread film is lifted above the surface due to rapid vapor film formation underneath the drop. Then the lifted film disintegrates into small droplets, which are larger than the droplets emitted at 200 °C. The droplet ejection is in radial direction rather than upward as seen in the case of 200 °C. The droplets have longer lifetime than those from impact at 200 °C due to their greater size. Although the vaporization process is different depending on target temperature, the high-speed images reveal that the initial spreading stages are identical to those from impact on room-temperature surface.

ACKNOWLEDGMENT

This work was supported by Combustion Engineering Research Center (CERC) at KAIST.

[1] A. M. Worthington, Proc. R. Soc. London **25**, 261 (1877); **25**, 498 (1877).
[2] S. Schiaffino and A. A. Sonin, Phys. Fluids **9**, 3172 (1997).
[3] S. T. Thoroddsen and K. Takehara, Phys. Fluids **12**, 1265 (2000).
[4] H.-Y. Kim and J.-H. Chun, Phys. Fluids **13**, 643 (2001).
[5] S. Chandra and C. T. Avedisian, Proc. R. Soc. London, Ser. A **432**, 13 (1991).
[6] S. T. Thoroddsen and J. Sakakibara, Phys. Fluids **10**, 1359 (1998).
[7] T. Mao, D. C. S. Kuhn, and H. Tran, AIChE J. **43**, 2169 (1997).
[8] R. Rioboo, M. Marengo, and C. Tropea, Exp. Fluids **33**, 112 (2002).
[9] Y.-S. Yang, H.-Y. Kim, and J.-H. Chun, IEEE Trans. Compon. Packag. Technol. **26**, 215 (2003).
[10] M. Al-Roub, P. V. Farrell, and J. Senda, SAE paper 960863 (1996).
[11] C.-A. Chen and J.-H. Chun, CIRP Ann. **46/1**, 131 (1997).
[12] D. Attinger, Z. Zhao, and D. Poulikakos, J. Heat Transfer **122**, 544 (2000).
[13] Lord Rayleigh, Proc. London Math. Soc. **10**, 4 (1897).
[14] W. L. Buehner, J. D. Hill, T. H. Williams, and J. W. Woods, IBM J. Res. Dev. **21**, 2 (1977).
[15] P. Yim, J.-H. Chun, T. Ando, and V. K. Sikka, Int. J. Powder Metall. **32**, 155 (1996).
[16] K. Asano, Y. Funayama, K. Yatsuzuka, and Y. Higashiyama, J. Electrost. **35**, 3 (1995).
[17] A. M. Sterling and C. A. Sleicher, J. Fluid Mech. **68**, 477 (1975).
[18] C. Weber, Z. Angew. Math. Mech. **11**, 136 (1931).
[19] J. M. Schneider, N. R. Lindblad, and C. D. Hendricks, J. Appl. Phys. **38**, 6 (1967).
[20] M. Orme, J. Courter, Q. Liu, C. Huang, and R. Smith, Phys. Fluids **12**, 2224 (2000).
[21] J. A. Mulholland, R. K. Srivastava, and J. O. L. Wendt, AIAA J. **26**, 1231 (1988).
[22] P. Mathur, D. Apelian, and A. Lawley, Acta Metall. **37**, 429 (1989).
[23] N. Hatta, H. Fujimoto, and H. Takuda, J. Fluids Eng. **117**, 394 (1995).
[24] H. Fujimoto, S. Ito, and I. Takezaki, Exp. Fluids **33**, 500 (2002).
[25] H. Ku, J. Res. Natl. Bur. Stand., Sect. C **70**, 263 (1966).
[26] L. H. J. Wachters and N. A. J. Westerling, Chem. Eng. Sci. **21**, 1047 (1966).
[27] J. Senda, K. Yamada, H. Fujimoto, and H. Miki, JSME Int. J. Ser. II **31**, 105 (1988).
[28] J. Senda and H. G. Fujimoto, Appl. Mech. Rev. **52**, 119 (1999).